catalysts

Article

Modification of $SmMn_2O_5$ Catalyst with Silver for Soot Oxidation: Ag Loading and Metal–Support Interactions

Baofang Jin [1], Yuxin Liu [1], Yue Ma [1], Zhenguo Li [2], Kaixiang Li [2], Shuang Liu [3], Rui Ran [1] and Xiaodong Wu [1,*]

[1] The Key Laboratory of Advanced Materials of Ministry of Education, School of Materials Science and Engineering, Tsinghua University, Beijing 100084, China; jinbaofang@163.com (B.J.); liuyuxin17@tsinghua.org.cn (Y.L.); yue.ma@tum.de (Y.M.); ranr@tsinghua.edu.cn (R.R.)
[2] National Engineering Laboratory for Mobile Source Emission Control Technology, China Automotive Technology & Research Center, Tianjin 300300, China; lizhenguo@catarc.ac.cn (Z.L.); likaixiang@catarc.ac.cn (K.L.)
[3] School of Materials Science and Engineering, Ocean University of China, Qingdao 266100, China; lius@ouc.edu.cn
* Correspondence: wuxiaodong@tsinghua.edu.cn; Tel.: +86-10-6279-2375

Abstract: A series of Ag-modified manganese-mullite ($SmMn_2O_5$) catalysts with different Ag contents (1, 3, and 6 wt.%) were prepared via a citric acid sol–gel method for catalytic soot oxidation. The catalysts were characterized by powder X-ray diffraction (XRD), Brunauer–Emmett–Teller (BET), Raman spectroscopy, transmission electron microscopy (TEM), high-resolution transmission electron microscopy analysis (HRTEM), X-ray photoelectron spectroscopy (XPS), and H_2 temperature-programmed reduction (H_2-TPR). The soot oxidation activity of the mullite was significantly promoted by the addition of silver and affected by the loading amount of the metal. Herein, the influences of silver loading on the metal size distribution and its interactions with the mullite were studied. Based on these characterizations, a possible soot oxidation reaction mechanism was proposed for silver-modified $SmMn_2O_5$.

Keywords: Mn-based mullite; Ag modification; soot oxidation; metal dispersion; metal–support interaction; oxygen activation

check for updates

Citation: Jin, B.; Liu, Y.; Ma, Y.; Li, Z.; Li, K.; Liu, S.; Ran, R.; Wu, X. Modification of $SmMn_2O_5$ Catalyst with Silver for Soot Oxidation: Ag Loading and Metal–Support Interactions. *Catalysts* **2024**, *14*, 135. https://doi.org/10.3390/catal14020135

Academic Editor: Avelina García-García

Received: 20 January 2024
Revised: 5 February 2024
Accepted: 6 February 2024
Published: 9 February 2024

1. Introduction

Diesel particulate matters (PM) pose a serious threat to the atmospheric environment and human health [1–3]. A catalytic diesel particulate filter (CDPF) has been considered as an efficient way to reduce diesel PM emissions [4,5]. PM from diesel exhaust gases can be removed through two processes. The first process is the capture of PM, which can be achieved by the wall-flow structure of the CDPF to capture PM effectively in the exhaust gas. When PM is accumulated to a certain extent, the captured PM needs to be burned clean. Then, the CDPF can continue to capture and oxidize the PM in the exhaust gas, i.e., the so-called passive regeneration process. The core of this technology is to develop highly efficient catalysts, which can convert soot, one of the most difficult oxidized components in the PM, to CO_2 at low temperatures. Pt-based materials have been widely used as commercial catalysts due to their high NO oxidation ability, which can promote soot oxidation through a NO_2-assisted mechanism [6–8]. However, Pt as a scarce metal is expensive. Therefore, there is an urgent need to seek alternatives with lower cost.

It has been reported that many non-noble metal oxides including Ce-based oxides [9,10], transition metal oxides [11–14], and alkaline metal oxides [8,15] are effective for soot oxidation. Among them, Mn-based metal oxides are one of the most promising soot oxidation catalysts due to their abundance, non-toxicity, and high activity. Single manganese oxides with different valence states are prone to sintering and phase changes at high temperatures [16]. By contrast, Mn-based composite oxides not only have superior catalytic activity

but also high thermal stability, especially Mn-based mullites. For example, Wang et al. [17] reported that Mn-mullite (Sm,Gd)Mn_2O_5 was able to oxidize NO in simulated diesel exhaust at temperatures as low as 75 °C, which is comparable with the commercial Pt/Al_2O_3 catalyst. Liu et al. [18]. synthesized $SmMn_2O_5$ by in situ dismutation of solid-state Mn^{3+} in bulk $SmMnO_3$ perovskite for catalytic oxidation of VOC and found that it exhibits excellent catalytic activity and stability. Chen et al. [19]. compared three kinds of Mn-based mullites ($SmMn_2O_5$, YMn_2O_5, and $PrMn_2O_5$) for NO oxidation and found that $SmMn_2O_5$ exhibited the best NO oxidation ability due to its abundant surface-adsorbed oxygen species and good reducibility.

Although Ag also belongs to noble metals, it has attracted widespread attention for catalytic oxidation reactions due to its relatively low price and high reactivity. Research has found that introducing Ag into metal oxides such as CeO_2 [20], MnO_2 [21], $MnCo_2O_4$ [22], and $LaMnO_3$ [23] is beneficial for activating oxygen species by accelerating dissociation of adsorbed O_2 and migration of lattice oxygen in the bulk of oxides. Due to its distinct characteristics, Ag exhibits potential application prospects in the catalytic oxidation of soot. Cui et al. [24] developed Ag-supported CoCe porous nanosheet catalysts for soot oxidation. They reported that the introduction of Ag significantly reduced the ignition temperature of the catalyst under a loose contact mode without the assistance of other exhaust gases such as NO_x, due to the good contact with soot and low energy barrier for O_2 dissociation. Chen et al. [25] reported that Ag/Co_3O_4 presented competitive catalytic activity toward soot combustion with a T_{50} (the temperature at soot conversion of 50%) below 290 °C in 10% O_2/N_2. They attributed the high activity of Ag/Co_3O_4 catalyst to the enhanced metal–support interaction induced by the formation of uniform, dispersive, and suitable sized metallic Ag nanoparticles. In our previous work [26,27], we also discovered that $SmMn_2O_5$ had good catalytic performance in oxidation of soot and VOCs. Additionally, the influence of preparation methods of silver on $SmMn_2O_5$ was also investigated. It was found that in situ introduction of Ag by a sol–gel method exhibited better catalytic activity than the impregnated one. However, the effect of Ag loading on the catalytic performance of the mullite remains unknown.

Following our previous method [26,27], this work synthesized a series of Ag-modified manganese-mullite catalysts with different Ag contents. As expected, introducing Ag significantly boosted soot oxidation. More importantly, we found that there was an optimal Ag loading to achieve a balance between Ag loading and Ag particle size. This work presents new insights into the interactions between $SmMn_2O_5$ mullite and silver by tuning the loading amount of the metal and developing catalyst candidates for oxidation reactions.

2. Results and Discussion

2.1. Characterization of Catalysts

2.1.1. XRD Analysis

The crystalline phases of the catalysts were characterized by XRD, and the results are shown in Figure 1. In Figure 1a, the XRD pattern of the SMO sample shows main diffraction peaks at 2θ values of 28.7°, 30.5°, 33.8°, 35.5°, and 41.3° corresponding to the (121), (211), (130), (112), and (212) planes of a typical mullite-type mixed oxides $SmMn_2O_5$. The introduction of Ag does not change the crystal structure of the catalyst. Additionally, the peak at 2θ = 33.2° attributed to the perovskite-type mixed oxides ($SmMnO_3$) can be detected, indicating the incomplete phase transformation from the perovskite to the mullite for all the samples. Although the diffraction peaks of Ag overlap partially with those of mullite, it can be observed by the slow scanning technique in Figure 1b that the diffraction peak at 2θ = 38.1° attributed to the metallic silver (111) plane increases significantly in intensity in the patterns of 3Ag/SMO and 6Ag/SMO catalysts, implying the aggregation and sintering of silver with increasing Ag loading.

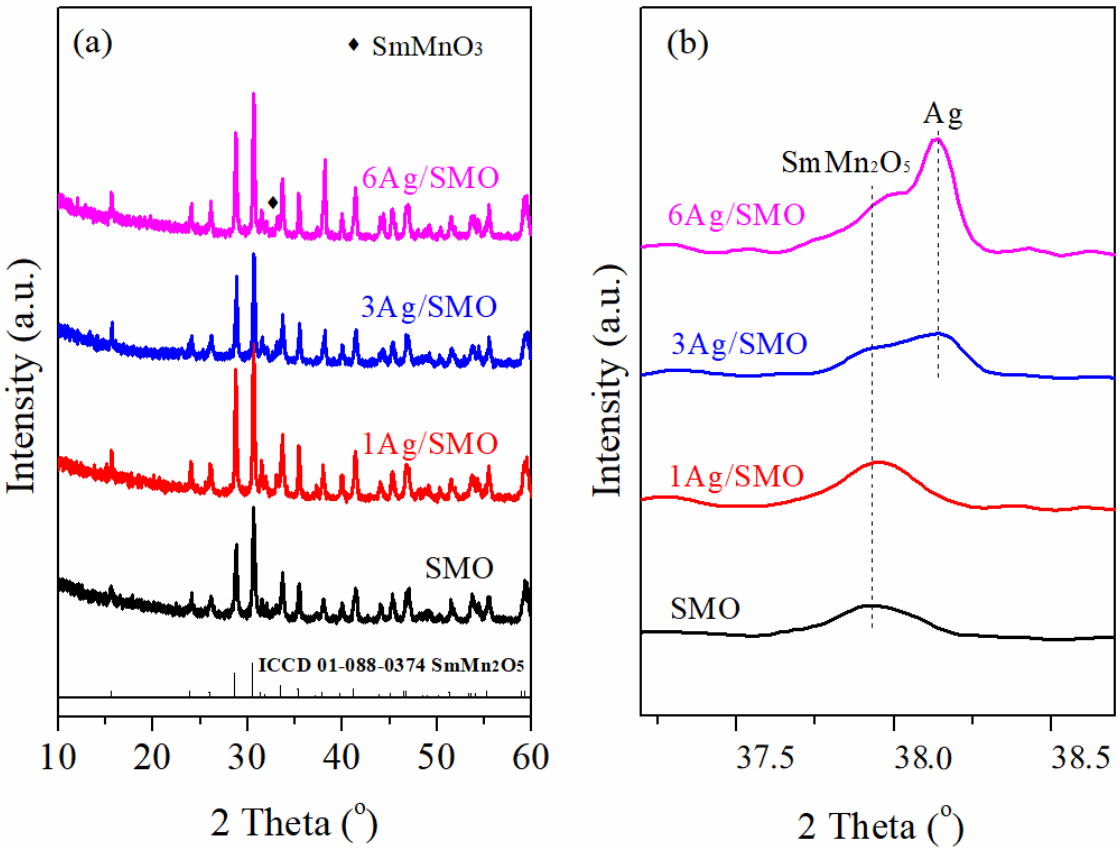

Figure 1. (**a**) Normal and (**b**) slow-scanning XRD patterns of the catalysts.

Table 1 lists the crystal cell parameters and the average crystallite sizes of $SmMn_2O_5$ over the catalysts. Compared with pure mullite, the addition of silver leads to a shrinkage of the mullite crystal cell, which may be related to the transformation of Mn^{3+} (with the ionic radii of 0.065 nm [28]) to Mn^{4+} (0.053 nm [29]) according to the charge balance law arising from the replacement of the Sm^{3+} (0.108 nm [30]) sites by Ag^{+} (0.115 nm [31]) in the mullite. Another possible explanation is the electron transfer from Mn^{3+} ions in the mullite to silver at the metal–support interface. At a high loading of 6 wt.%, the aggregation and sintering of silver weakens its interaction with the mullite, resulting in an expansion of the mullite crystal cell again. Overall, the greatest crystal cell shrinkage occurs over 3Ag/SMO, implying the maximum lattice distortion in the mullite resulting from the addition of 3 wt.% silver. Additionally, the introduction of Ag accelerates the sintering of the mullite, with the average crystallite size increasing from 30 to ca. 40 nm. Correspondingly, the specific surface areas of the SMO, 1Ag/SMO, 3Ag/SMO, and 6Ag/SMO catalysts are 16.2, 13.7, 10.6, and 11.7 $m^2\ g^{-1}$, respectively, indicating that the sintering of the mullite crystallites and loss of the textural feature of the Ag-containing catalysts assisted with the metal.

Table 1. Structural and textural properties of the catalysts.

Catalyst	Cell Parameter [a]				$d_{SmMn2O5}$ [b] (nm)	S_{BET} [c] (m^2/g)
	a (nm)	b (nm)	c (nm)	a × b × c (nm^3)		
SMO	0.7502	0.8503	0.5704	0.3638	30.4	16.2
1Ag/SMO	0.7477	0.8548	0.5665	0.3620	39.5	13.7
3Ag/SMO	0.7429	0.8525	0.5662	0.3585	40.4	10.6
6Ag/SMO	0.7455	0.8530	0.5686	0.3615	40.3	11.7

[a] The lattice constants estimated from consecutive peaks using the Bragg formula. [b] Crystallite size of the mullite calculated by Debye–Scherrer equation. [c] Surface area derived from the BET equation.

2.1.2. Raman Analysis

Raman spectroscopy is a powerful technique for characterizing the molecular structure of the materials. To further evaluate the effect of Ag addition on M-O bonds in the mullite, Raman spectroscopy was performed and the results are shown in Figure 2. Both the peaks at 612.1 and 678.5 cm^{-1} are assigned to Mn-O stretching vibrations, which shift towards lower frequencies and are strengthened in intensity after introduction of Ag. These peak shifts are closely related to the changes in lattice defects as reported by Wang's work [32], suggesting the prolonged Mn-O bond and the shared lattice oxygen in the mullite with Ag species. The highest shifts appear in the Raman peaks of 3Ag/SMO due to the creation of more lattice defects, which agrees with the variations in crystal cell parameters obtained by XRD.

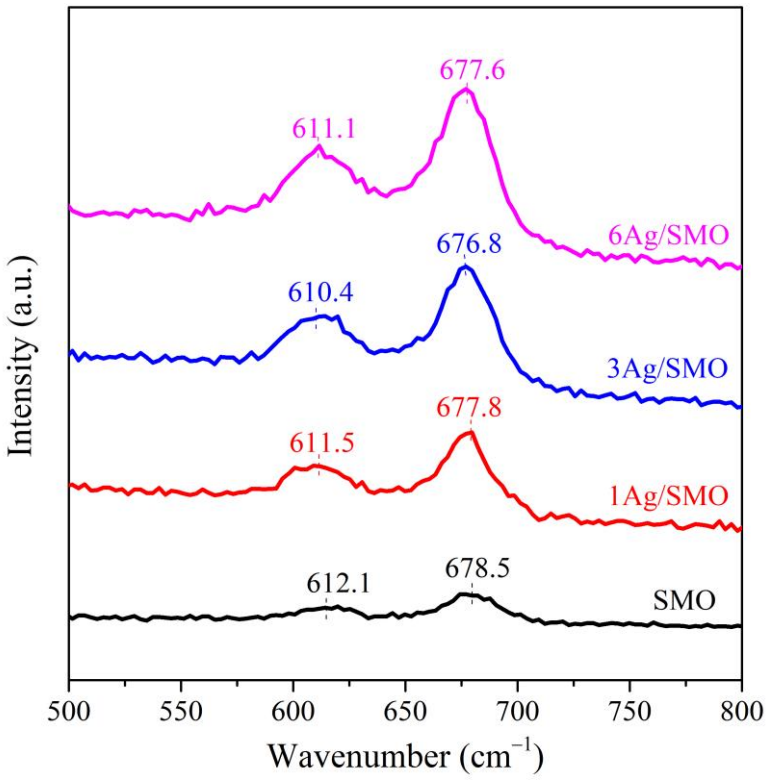

Figure 2. Raman spectra of the catalysts.

2.1.3. TEM Observation

TEM can be utilized to observe the morphology of the catalysts and determine the size distribution of silver, and the results are shown in Figure 3a,c,e,g. It can be observed in Figure 3a that SMO consists of aggregated nanoparticles. As the solid was obtained by calcination at 800 °C for 5 h, aggregation between nanoparticles occurred significantly, which leads to the reduction of the free surface with the secondary elimination of the grain boundary area and low specific surface area of the mixed oxides. To further confirm the lattice spacing of the catalyst, HRTEM was conducted. As shown in Figure 3b, the mullite is well crystallized. The measured lattice fringes are 0.279 and 0.287 nm, corresponding to the (220) and (002) planes of $SmMn_2O_5$, respectively. All the Ag-containing catalysts (Figure 3c,e,g) show similar morphology with larger mullite particle size. The lattice fringes of 0.235 nm corresponding to the Ag (111) facet can be clearly observed in these Ag-containing catalysts (Figure 3d,f,h). A total of 100–150 silver nanoparticles were measured for size distribution statistics of each sample and the results are shown in the inserted figures. The average Ag nanoparticle size is 2.53, 3.49 and 5.64 nm for 1Ag/SMO, 3Ag/SMO and 6Ag/SMO, respectively. Clearly, the average size of Ag nanoparticles increases with the metal loading, agreeing with the XRD results.

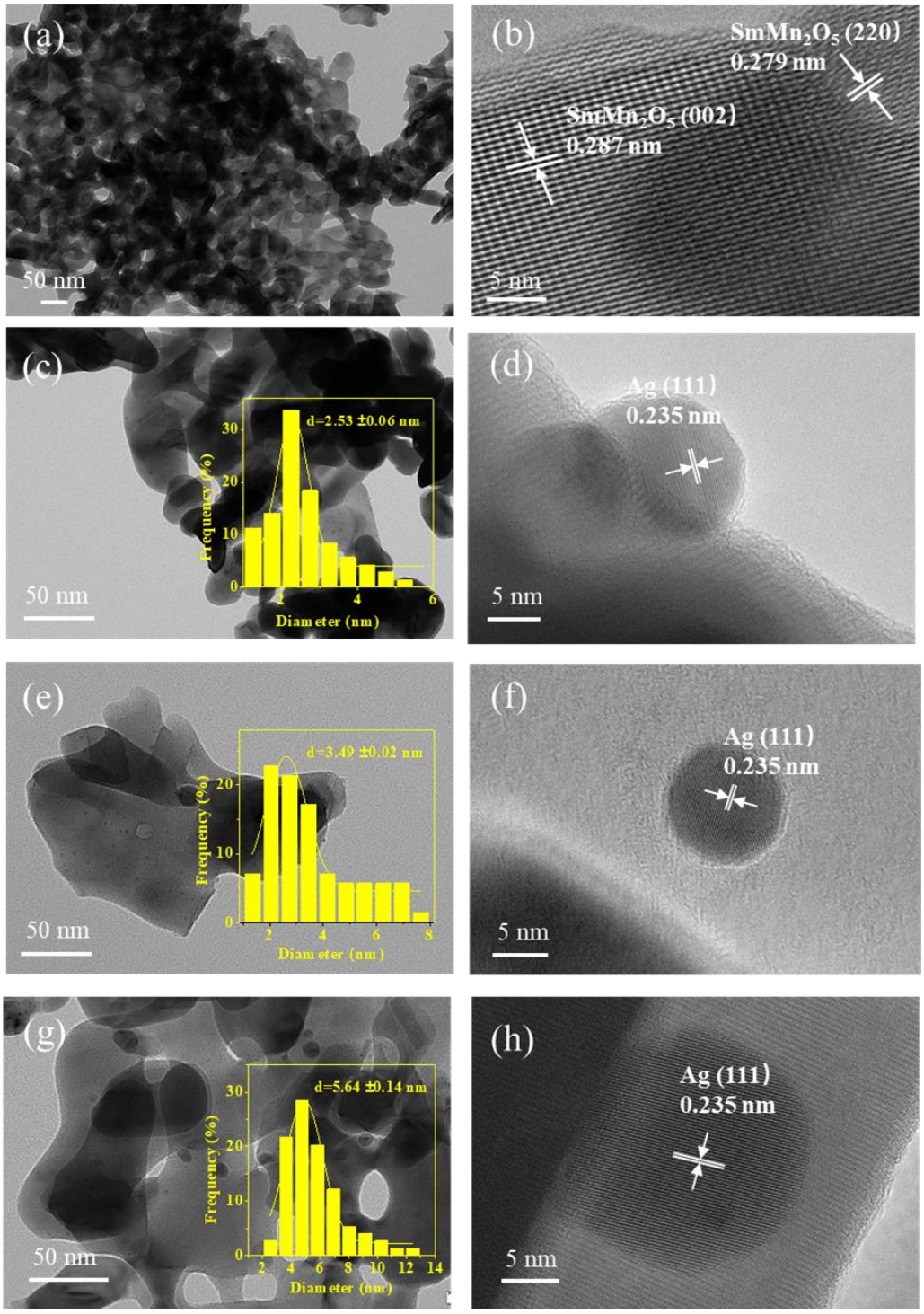

Figure 3. TEM and HRTEM images of (**a**,**b**) SMO, (**c**,**d**) 1Ag/SMO, (**e**,**f**) 3Ag/SMO, and (**g**,**h**) 6Ag/SMO.

2.1.4. XPS Analysis

XPS can be used to detect the elementary composition and elemental chemical state of the catalysts, and the results are shown in Figure 4. The XPS peaks at 641.5 and 653.0 eV in Figure 4a, corresponding to the binding energies (BE) of Mn $2p_{3/2}$ and $2p_{1/2}$ levels, can be assigned to Mn^{3+}, while the other two peaks located at 642.7 and 654.2 eV are attributed to Mn^{4+} [27,33]. The Mn^{4+}/Mn^{3+} ratio was calculated by deconvoluting the Mn 2p XPS spectra and the results are listed in Table 2. Compared with pure mullite, the introduction of silver results in an increase in the Mn^{4+}/Mn^{3+} ratio, which agrees with the

XRD results about shrinkage of crystal cell. However, the Mn^{4+}/Mn^{3+} ratio varies little for the Ag-modified catalysts. This is probably because of the formation of large Ag particles with increasing Ag loading, which weaken the interactions between the metal and the mullite support.

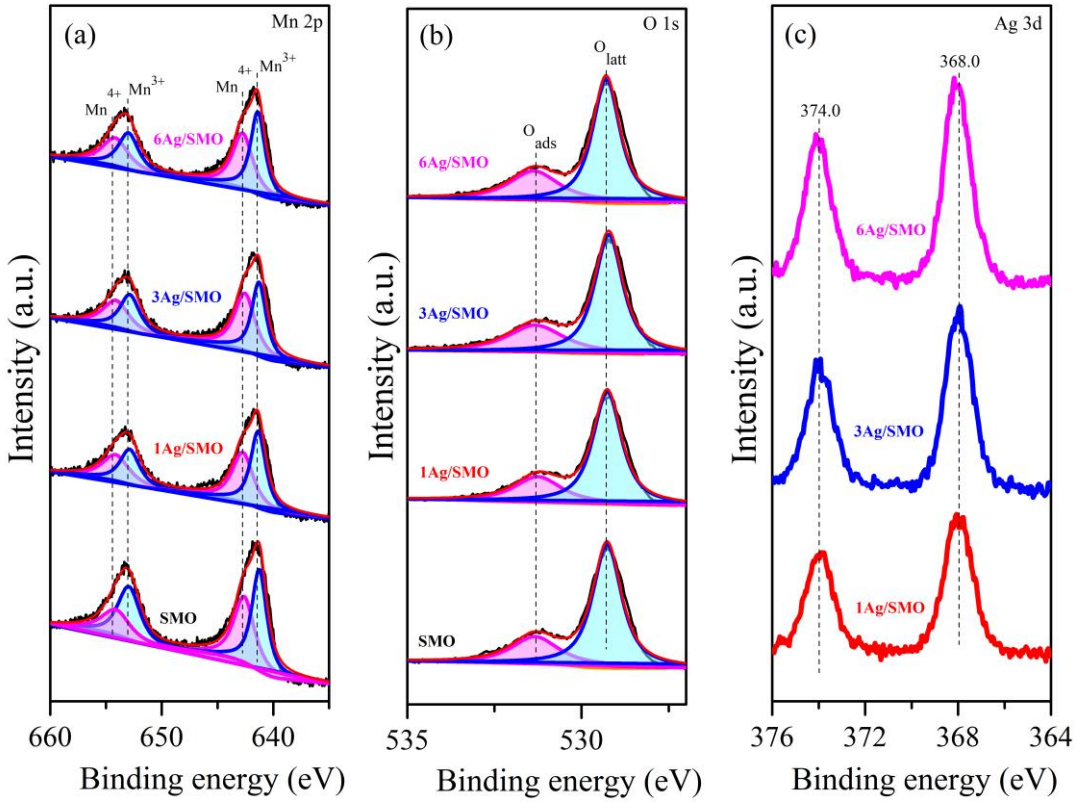

Figure 4. (**a**) Mn 2p, (**b**) O 1s and (**c**) Ag 3d XPS spectra of the catalysts.

Table 2. Surface elemental contents of the catalysts.

Catalyst	Surface Content (wt.%) [a]				Mn^{4+}/Mn^{3+} [a]	O_{ads}/O_{latt} [a]	$Mn^{4+}/(Mn^{4+} + Mn^{3+})$ [b]
	Sm	Mn	O	Ag			
SMO	40.2	32.4	27.4	---	0.53	0.48	0.43
1Ag/SMO	40.4	28.5	24.8	6.3	0.70	0.63	0.69
3Ag/SMO	38.2	28.1	26.1	7.6	0.73	0.65	0.74
6Ag/SMO	38.7	27.3	25.8	8.2	0.71	0.62	0.70

[a] Calculated from XPS data. [b] Estimated from H_2-TPR results.

The O 1s spectra were fitted into two peaks in Figure 4b. The higher binding energy peak at 531.3 eV is assigned to chemisorbed oxygen (O_{ads}), while the lower binding energy one at 529.3 eV is assigned to lattice oxygen (O_{latt}) [34]. As listed in Table 2, the introduction of Ag increases the O_{ads}/O_{latt} ratio, arising from the generation of lattice defects accompanied with the significantly increased Mn^{4+}/Mn^{3+} ratio. Among the prepared catalysts, 3Ag/SMO exhibits the highest Mn^{4+}/Mn^{3+} and O_{ads}/O_{latt} ratios, although the differences are not obvious. These implies the strongest interactions between the metal and the support over this catalyst.

The Ag 3d XPS spectra are shown in Figure 4c. Ag exists in the form of metallic Ag^0, with the Ag $3d_{5/2}$ and Ag $3d_{3/2}$ peaks at 368.0 and 374.0 eV [35], respectively, which agrees well with the HRTEM and XRD results. It is interesting to note in Table 2 that the surface contents of Ag on the catalysts by XPS are higher than their nominal Ag contents, resulting

from the enrichment of the metal on the mullite surface. Although the nominal Ag contents in Ag/SMO are in multiple relations, the surface contents of Ag on *x*Ag/SMO are close to each other. As is well-known, XPS measurements are influenced by some factors, such as the probing depth (generally a few nanometers), the distribution of the aimed elements, and the sample homogeneity. In this work, the size of Ag nanoparticles in Ag/SMO increases with increasing Ag content according to the HRTEM results. Relatively large Ag nanoparticles and poor dispersion of Ag in 6Ag/SMO results in incomplete detection of surface Ag by XPS. Therefore, the obtained surface Ag content on Ag/SMO does not increase significantly along with their nominal loadings. Similar phenomena have been previously reported [27,36].

2.1.5. H_2-TPR Analysis

The redox property of catalysts is crucial to the catalytic oxidation of soot. H_2-TPR characterization was used to determine the redox properties of catalysts, and the results are shown in Figure 5. The overlapped peaks were fitted by Gaussian curves. It can be seen that SMO mainly exhibits four reduction peaks at 251.5, 319.5, 382.5, and 418.2 °C. The first two peaks are ascribed to the reduction of surface-adsorbed oxygen and the reduction of Mn^{4+} to Mn^{3+} in the mullite, respectively. The last two peaks are both ascribed to the reduction of Mn^{3+} to Mn^{2+}, maybe due to the different coordination environments of Mn atoms in the mullite. The introduction of Ag significantly promotes the reduction of the mullite, with the reduction peaks shifting towards lower temperatures by more than one hundred degrees centigrade. For 1Ag/SMO, the peak at 182.1 °C is attributed to the reduction of surface-adsorbed oxygen. The peaks at 246.6 and 286.7 °C are attributed to the successive reduction of Mn^{4+} and Mn^{3+} in the mullite promoted by silver, while the small peak at 325.3 °C may be attributed to the reduction of Mn^{3+} in the mullite without interaction with silver [27]. Apparently, it can be seen that the relative peak area ratio of Mn^{4+} to (Mn^{4+} + Mn^{3+}) reaches the maximum over 3Ag/SMO, indicating the strongest promotion effect of silver on the reducibility of the mullite. As listed in Table 2, the Mn^{4+}/Mn ratio follows the order of SMO (0.43) < 1Ag/SMO (0.69) < 6Ag/SMO (0.70) < 3Ag/SMO (0.74), suggesting that introducing Ag increases the content of high-valent Mn^{4+} significantly. However, at a higher Ag loading, the interactions between the metal and the mullite is weakened in 6Ag/SMO due to the aggregation of segregated metal.

2.2. Catalytic Activity for Soot Oxidation

The catalytic activity of the catalysts for soot oxidation under loose contact between soot and the catalyst was evaluated. Figure 6a shows the soot conversion profiles of the catalysts in the presence of NO as a function of temperature, and Table 3 lists the corresponding values of T_{10}, T_{50} and T_{90} for soot oxidation. It was found that compared with SMO, all the Ag-containing catalysts behaves much better in the soot conversion within the whole temperature range due to their superior redox properties. Among these modified catalysts, 3Ag/SMO exhibits some advantage especially at the soot catalytic ignition stage, achieving the lowest T_{10}. Both the mullite and Ag-containing catalysts exhibit high CO_2 selectivity (S_{CO2} > 99.5%) during soot oxidation, which can effectively avoid the generation of secondary pollutants such as CO. Additionally, the NO_2 production over Ag-containing catalysts, taking 3%Ag/SMO as an example, during the TPO runs of NO and soot oxidation is shown in Figure 6b. The NO_2 concentration during the NO-TPO is higher than that obtained during the soot-TPO tests at the temperatures above 220 °C, which is due to the consumption of NO_2 by reacting with soot. The catalytic performance of this material was similar to those modified $SmMn_2O_5$ [37–39] and superior to those of many other previously reported compounds, such as Ag [40,41], Pt [42,43], Pd [44], Cu [45], and Ce-based catalysts [15,46,47], as briefly summarized in Table S1. The reusability of the catalysts was evaluated via a cycled soot-TPO test, taking 3%Ag/SMO as an example (Figure S1). Compared with the fresh catalyst, the used counterparts even exhibit somewhat

improved activity in O_2, maybe due to the redispersion of the metal on the mullite during the TPO runs.

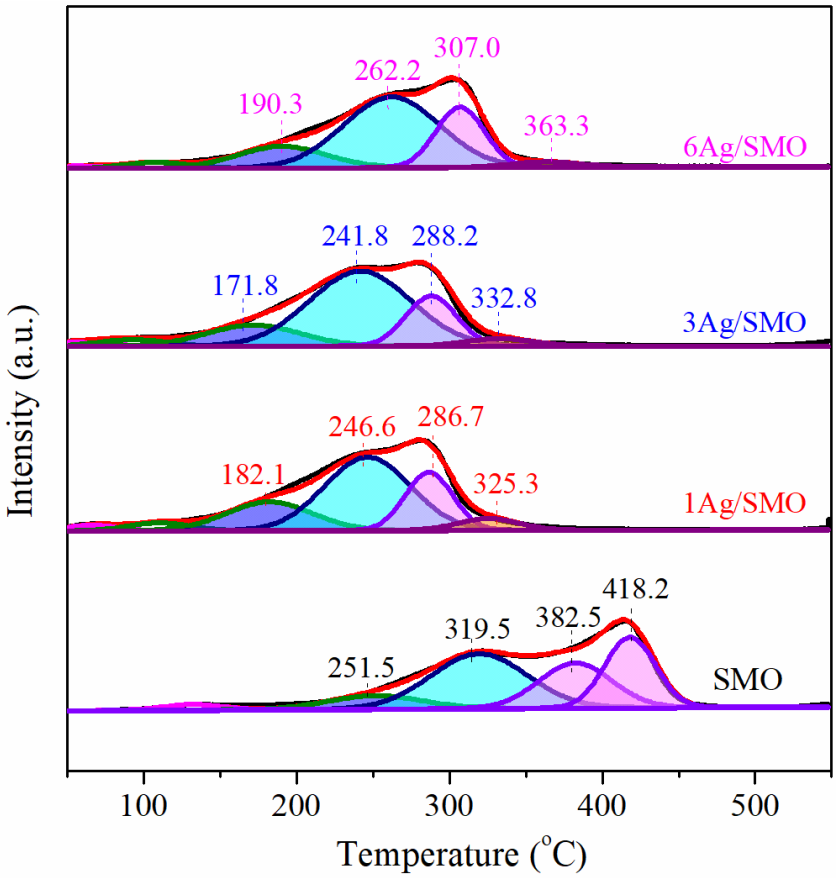

Figure 5. H_2-TPR profiles of the catalysts.

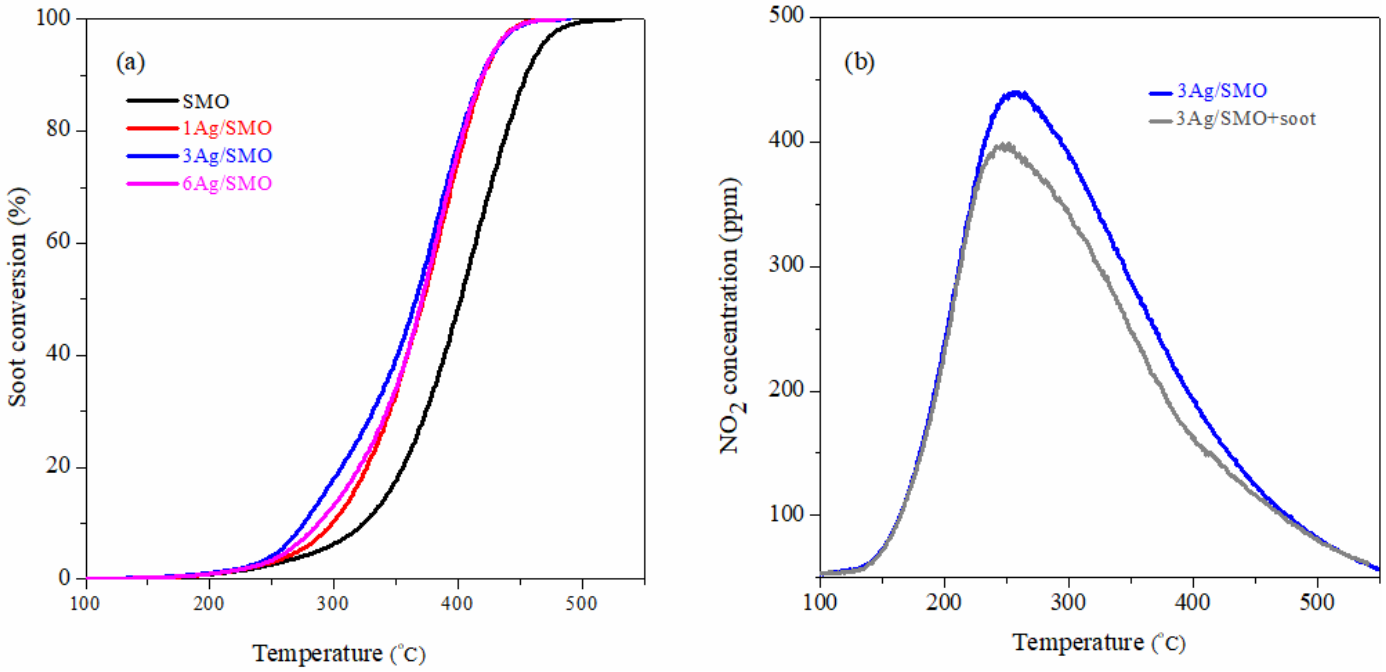

Figure 6. (**a**) Soot conversion over the catalysts during soot-TPO and (**b**) NO_2 production over a representative 3Ag/SMO during NO- and soot-TPO tests. Reactant gas: 500 ppm NO/10% O_2/N_2.

Table 3. Catalytic features of the catalysts for soot oxidation.

Catalyst	T_{10} (°C)	T_{50} (°C)	T_{90} (°C)	S_{CO2} (%)
SMO	323	403	456	99.4
1% Ag/SMO	300	372	420	99.7
3% Ag/SMO	278	367	420	99.8
6% Ag/SMO	290	372	421	99.9

2.3. The Proposed Reaction Mechanism

Based on the above results and previous studies, a possible soot oxidation reaction mechanism over Ag/SMO is proposed in Figure 7. During reactions in the presence of O_2 and NO, NO interacts with active oxygen species provided by the activation of oxygen vacancies in the mullite and especially dissociation of gaseous oxygen on silver nanoparticles, resulting in the formation of NO_2. As is well known, NO_2 has stronger oxidizing ability than O_2, which can directly oxidize soot. As evidenced by the difference in NO_2 concentration between NO-TPO and soot-TPO results (Figure 6b), the consumption of NO_2 indicates its involvement in the oxidation of soot, known as the NO_2-assisted soot oxidation mechanism. After the loading of Ag in SMO, the reducibility and catalytic activity of the catalysts are improved remarkably. This suggests that the introduction of Ag plays critical roles for soot oxidation. On the one hand, Ag with low work function could stimulate the lattice oxygen in the mullite support with abundant oxygen vacancies via back spillover effect to produce active oxygen species [48,49], leading to a favorable environment for NO and soot oxidation. On the other hand, gaseous O_2 can be adsorbed on the Ag sites and dissociated into atomic oxygen efficiently [48–50]. During these processes, the loading content of Ag is crucial to the amount and reactivity of active sites by affecting the particle size of Ag and the interactions between Ag and the mullite. The lower the Ag loading, the smaller the metal particle size, which facilitates the oxygen activation and interaction with the mullite. At a low content of Ag, it is not sufficient for 1Ag/SMO to produce sufficient active oxygen species and high valence Mn^{4+} in the mullite. At a much higher Ag loading, the aggregation and sintering of the metal weaken the interactions with the mullite, resulting in a decrease in redox ability of 6Ag/SMO catalyst. Therefore, a proper Ag loading such as 3 wt.% enables the catalyst with sufficient active sites with high reactivity and thereby the lowest soot ignition temperature T_{10} (Table 3).

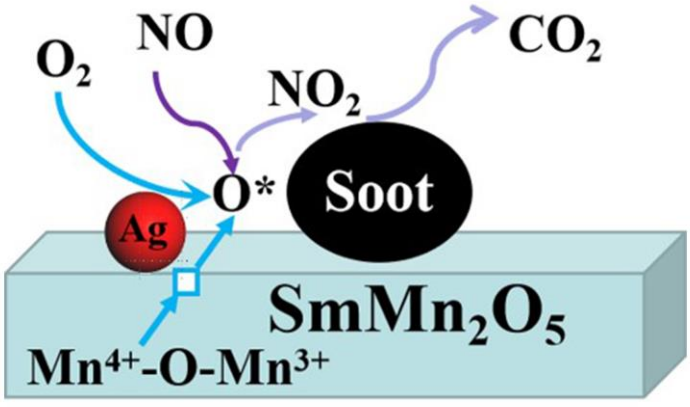

Figure 7. Schematic illustration of soot oxidation over Ag/SMO catalysts. The rectangle and O* represent oxygen vacancies and active oxygen species, respectively.

3. Experimental

3.1. Chemicals and Materials

All analytical-grade chemicals were used without further purification. Samarium nitrate hexahydrate ($Sm(NO_3)_3 \cdot 2H_2O$, 99.99%), manganese nitrate solution ($Mn(NO_3)_3$, 50%), citric acid monohydrate ($C_6H_{10}O_8$, 99.5%), and silver nitrate ($AgNO_3$, 9.5%) were

purchased from Aladdin Reagent Co., Ltd., Shanghai, China. High-purity nitrogen (N_2, ≥99.999%), nitric oxide standard gas (NO, 1%) mixed with the base gas of highly pure nitrogen, and synthetic air were purchased from Beijing Praxis Practical Gases Co., Ltd., Beijing, China. Deionized water was obtained from a Millipore water purification system (Darmstadt, Germany).

3.2. Catalyst Preparation

Manganese-mullite $SmMn_2O_5$ was prepared by a facile citric acid sol–gel method. In a typical preparation, stoichiometric $Sm(NO_3)_3$, $Mn(NO_3)_3$, and citric acid were mixed in deionized water under stirring to form a homogeneous solution at room temperature. To ensure complete complexation of the metal ions, the molar ratio of citric acid and total metal nitrates in the solution was 1.1:1. The mixed solution was then heated to 90 °C and continuously stirred. After evaporation of water, a dark brown gel formed. The gel was dried at 110 °C overnight to form a spongy amorphous solid. The obtained solid was heated to 800 °C at a rate of 1 °C min^{-1} and kept for 5 h. The obtained mullite was denoted as SMO. Ag-modified SMO catalysts (xAg/SMO) with various Ag to SMO mass ratios (1:100, 3:100, and 6:100) were also prepared using the same method with additional additive of $AgNO_3$ as one of the precursors and these solids were calcined at 800 °C for 5 h. The obtained catalysts were denoted as 1Ag/SMO, 3Ag/SMO, and 6Ag/SMO, respectively.

3.3. Characterizations

X-ray diffraction (XRD) was carried out on a Bruker D8 Advance (Billerica, MA, USA) operating at 40 kV and 10 mA and using Cu Kα radiation (λ = 1.54184 Å), and the XRD patterns were collected in a 2θ range of 10° to 60° at a scanning rate of 6°/min. In addition, slow scanning XRD analysis was performed in the range 30° to 40° at a scanning rate of 1°/min. The crystallite size of mullite was calculated by Scherrer equation.

N_2 adsorption/desorption measurement was carried out at −196 °C using a JW-BK122 F (Beijing JWGB, Beijing, China) instrument. Prior to the analysis, the samples were degassed at 220 °C under vacuum for 1 h. The specific surface area of the samples was obtained from the Brunauer–Emmett–Teller (BET) theory in the relative pressure (p/p_0) range of 0.05–0.30.

Raman spectra of the solids were recorded on a confocal micro-Raman spectrometer (IDSpec Aurora, Hong Kong, China) under ambient conditions. Prior to the analysis, the samples were fixed on a glass slide, and the slide was then placed onto the platform of the microscopy. After the laser beam was focused onto the sample surface, the Raman spectra were excited by a detective laser of 632.8 nm and recorded in the region of 500–800 cm^{-1}.

The morphology of the samples was characterized by transmission electron microscopy (TEM) (JEOL-2100, JEOL, Tokyo, Japan) operated at an accelerating voltage of 200 kV. High-resolution transmission electron microscopy analysis (HRTEM) (JEOL-2100, JEOL, Tokyo, Japan) of the samples was further carried out with a point resolution of 0.19 nm.

X-ray photoelectron spectroscopy (XPS) analysis was performed on an ESCALAB 250 Xi system (Thermo Fisher Scientific, Waltham, MA, USA) equipped with monochromatic Al Kα (1486.6 eV) X-ray source. The elemental composition of the catalyst was derived through a simple conversion formula according to the atomic ratios given by XPS without applying any standardization procedure. To obtain more information of Mn and O species, the obtained XPS spectra were deconvoluted employing the XPSPEAK41 software (version 4.1) after deducting the background signals using the Shirley algorithm. The C 1s line of adventitious hydrocarbon on air exposed samples with a binding energy of 284.6 eV was used as the reference to calibrate the XPS results.

H_2 temperature-programmed reduction (H_2-TPR) analysis was performed using a chemisorption analyzer (Micromeritics Auto Chem II 2920, Norcross, GA, USA) for the characterization of the redox properties of the catalysts. For each measurement, 0.05 g of catalyst was loaded into a quartz U-tube. Before the measurement, the catalyst was heated from room temperature to 300 °C at a rate of 10 °C·min^{-1} and kept in a stream of

air (20 mL/min) for 1 h. After cooling to 50 °C, the gas was switched to 10 vol. % H_2/Ar, and then the catalyst was heated to 900 °C at a rate of 10 °C·min^{-1} under this atmosphere (30 mL·min^{-1}). During the tests, the H_2 consumption was monitored as a TCD signal by the chemisorption analyzer.

3.4. Catalytic Activity Measurements

The catalytic oxidation of soot was tested in a home-made fixed-bed quartz reactor using a temperature-programmed oxidation (TPO) program at a heating rate of 5 °C/min from room temperature to 600 °C. Printex-U (diameter 25 nm, surface area 100 m^2/g, Degussa AG, Dusseldorf, Germany) was used as the model soot. Prior to the measurements, 10 mg soot and 100 mg catalyst were mixed using a spatula for 3 min to simulate a "loose contact" condition. To prevent reaction runaway, 0.3 g silica was then added to the mixture of soot and catalyst. The above mixtures were always sandwiched by two layers of quartz wool before put into the reactor. The inlet gas mixture containing 500 ppm NO and 10% O_2 balanced with N_2 was introduced into the reactor. The total flow rate of the feed mixture was 500 mL min^{-1} and the gas hourly space velocity (GHSV) was 100,000 h^{-1}. Before heating the reaction tube, the gas concentration needed to achieve stable. The effluent gas stream from the reactor was analyzed online by an infrared spectrometer (Nicolet iS10, Thermo Fisher Scientific, Waltham, MA, USA). The temperatures at the soot conversion of 10%, 50%, and 90% were defined as the T_{10}, T_{50} and T_{90}, respectively. Temperature-programmed oxidation of NO over the catalysts was also carried out on the same apparatus and steps without adding soot. The selectivity to CO_2 during soot oxidation (S_{CO2}) was expressed as another important factor by the equation $S_{CO2} = C_{CO2}/(C_{CO} + C_{CO2})$. C_{CO} and C_{CO2} were defined as the total CO and CO_2 released in the outlet gas during the soot-TPO test, respectively, which were obtained by integrating the outlet CO_x concentrations over time.

4. Conclusions

In this work, a series of Ag-modified mullite catalysts (xAg/SMO, x = 1, 3 and 6) with varied metal loadings were synthesized by the citric acid sol–gel method. Compared with pure mullite, the modified catalysts, especially 3Ag/SMO, exhibit significantly improved activity for soot oxidation in the presence of NO. Introduction of Ag increases the high-valence Mn^{4+} content and active adsorbed oxygen species in the mullite, leading to enhanced reducibility. Excessive loading of Ag, however, results in the formation of large Ag nanoparticles and weakened interactions of the metal with the mullite. Therefore, an appropriate Ag loading for $SmMn_2O_5$, which balances the amount and reactivity of Ag active species, is crucial to the catalytic oxidation of diesel soot. We hope this work can provide some theoretical foundations for the development of efficient soot oxidation catalysts operating at exhaust temperatures.

Supplementary Materials: The following supporting information can be downloaded at https://www.mdpi.com/article/10.3390/catal14020135/s1, Table S1: Comparative studies of catalytic activity for soot oxidation among various materials and our designed catalysts [15,37–47]; Figure S1: Cycled soot oxidation profiles of 3Ag/SMO. Reaction conditions: 10% O_2/N_2, GHSV = 100,000 h^{-1}, heating rate = 5 °C/min [51–54]; Figure S2: C 1s spectra for the catalysts [40].

Author Contributions: Conceptualization, B.J. and X.W.; data curation, B.J., Y.L. and X.W.; formal analysis, B.J., Y.M. and Z.L.; funding acquisition, X.W. and B.J.; investigation, B.J. and S.L.; methodology, X.W.; project administration, R.R.; resources, Z.L., K.L. and R.R.; supervision, X.W.; visualization, Z.L. and K.L.; validation, Y.L.; writing—original draft, B.J.; writing—review and editing, B.J., X.W., Y.L., Y.M., Z.L. and K.L. All authors have read and agreed to the published version of the manuscript.

Funding: This work was financially supported by projects of the National Key Research and Development Program of China (No. 2023YFC3707202), the National Natural Science Foundation of China (Grant No. 21906091), and Mobile Source Emission Control Technology (NELMS2020A08).

Data Availability Statement: Data are contained within the article and supplementary materials.

Conflicts of Interest: The authors declare no conflicts of interest.

References

1. Zhang, Y.; Pei, Y.; Liu, Q.; Gao, Y.; Min, K.; Chen, Z.; Shu, Z.; Liu, Q.; Zhou, Q.; Jiang, G. Tracing the plasma kallikrein-kinin system-activating component in the atmospheric particulate matter with different origins. *J. Hazard. Mater.* **2023**, *458*, 132044. [CrossRef] [PubMed]
2. Islam, N.; Saikia, B. An overview on atmospheric carbonaceous particulate matter into carbon nanomaterials: A new approach for air pollution mitigation. *Chemosphere* **2022**, *303*, 135027. [CrossRef] [PubMed]
3. Lee, E.; Lee, K.Y. NO_x-assisted soot oxidation with alkaline-earth metals (Ca, Sr, Ba) loaded on $Ag/2MnO_{x-1}CeO_2$. *J. Environ. Chem. Eng.* **2023**, *11*, 111312. [CrossRef]
4. Zhang, Y.; Lou, D.; Tan, P.; Hu, Z. Study of spatial and temporal aging characteristic of catalyzed diesel particulate filter catalytic performance used for diesel vehicle. *Sci. Rep.* **2020**, *10*, 19761. [CrossRef]
5. Zheng, C.; Wu, X.; Li, Z.; Ran, R.; Weng, D. Enhanced soot oxidation activity of a CuO-doped CeO_2 catalyst via acid etching. *Catalysts* **2023**, *13*, 1463. [CrossRef]
6. Wang, L.; Yu, D.; Zhao, Z.; Yu, X.; Li, D.; Zhou, S.; Zhong, C.; Hou, J.; Yin, C.; Fan, X. Simultaneous removal of soot and NO_x from diesel engines over three-dimensionally ordered macroporous ZSM-5-supported $MMnO_\delta$ Catalysts. *Ind. Eng. Chem. Res.* **2023**, *62*, 21950–21966. [CrossRef]
7. Torregrosa-Rivero, V.; Sanchez-Adsuar, M.S.; Illan-Gomez, M.J. Improving the performance of $BaMnO_3$ perovskite as soot oxidation catalyst using carbon black during sol-gel synthesis. *Nanomaterials* **2022**, *12*, 219. [CrossRef]
8. Yu, G.; Wang, J.; Ma, H.; Liu, X.; Qin, S.; Yang, Z.; Zhang, G.; Li, Y.; Zhu, L. Exploring abundantly synergic effects of K-Cu supported paper catalysts using TiO_2-ZrO_2 mesoporous fibers as matrix towards soot efficient oxidation. *Chem. Eng. J.* **2021**, *417*, 128111. [CrossRef]
9. Sacco, N.A.; Bortolozzi, J.P.; Milt, V.G.; Miró, E.E.; Banús, E.D. One step citric acid-assisted synthesis of Mn-Ce mixed oxides and their application to diesel soot combustion. *Fuel* **2022**, *322*, 124201. [CrossRef]
10. Bueno-López, A. Diesel soot combustion ceria catalysts. *Appl. Catal. B Environ.* **2014**, *146*, 1–11. [CrossRef]
11. Gao, Y.; Jin, B.; Wu, X.; Li, Z.; Ran, R.; Weng, D. Co-Precipitated $Mn_{0.15}Ce_{0.85}O_{2-\delta}$ catalysts for NO oxidation: Manganese precursors and Mn-Ce interactions. *Processes* **2022**, *10*, 2562. [CrossRef]
12. Cao, C.; Yang, H.; Xiao, J.; Yang, X.; Ren, B.; Xu, L.; Liu, G.; Li, X. Catalytic diesel soot elimination over potassium promoted transition metal oxide (Co/Mn/Fe) nanosheets monolithic catalysts. *Fuel* **2021**, *305*, 121446. [CrossRef]
13. Portillo-Vélez, N.S.; Zanella, R. Comparative study of transition metal (Mn, Fe or Co) catalysts supported on titania: Effect of Au nanoparticles addition towards CO oxidation and soot combustion reactions. *Chem. Eng. J.* **2020**, *385*, 123848. [CrossRef]
14. He, J.; Yao, P.; Qiu, J.; Zhang, H.; Jiao, Y.; Wang, J.; Chen, Y. Enhancement effect of oxygen mobility over $Ce_{0.5}Zr_{0.5}O_2$ catalysts doped by multivalent metal oxides for soot combustion. *Fuel* **2021**, *286*, 119359. [CrossRef]
15. Guan, B.; Huang, Y.; Lin, H.; Huang, Z. Promoting effects of barium substitution on the catalytic performances of $FeCeO_{2-\delta}$ for soot oxidation. *Ind. Eng. Chem. Res.* **2018**, *57*, 8635–8646. [CrossRef]
16. Mane, R.; Kim, H.; Han, K.; Kim, K.-J.; Soo Lee, S.; Roh, H.-S.; Lee, C.; Jeon, Y. Pivotal role of MnO_x physicochemical structure in soot oxidation activity. *Fuel* **2023**, *346*, 128287. [CrossRef]
17. Wang, W.; Mccool, G.; Kapur, N.; Yuan, G.; Shan, B.; Nguyen, M.; Graham, U.; Davis, B.; Jacobs, G.; Cho, K.; et al. Mixed-phase oxide catalyst based on Mn-mullite (Sm, Gd)Mn_2O_5 for NO oxidation in diesel exhaust. *Science* **2012**, *337*, 832–835. [CrossRef] [PubMed]
18. Liu, R.; Zhou, B.; Liu, L.; Zhang, Y.; Chen, Y.; Zhang, Q.; Yang, M.; Hu, L.; Wang, M.; Tang, Y. Enhanced catalytic oxidation of VOCs over porous Mn-based mullite synthesized by in-situ dismutation. *J. Colloid Interface Sci.* **2021**, *585*, 302–311. [CrossRef] [PubMed]
19. Chen, L.; Zhang, C.; Wu, T.; Huang, B.; Zhang, J.; Guan, G.; Zhang, Z.; Hou, X.; Hu, C.; Lu, Q. Effects of A-site replacement (Sm, Y, and Pr) on catalytic performances of mullite catalysts for NO oxidation. *Fuel* **2023**, *337*, 126838. [CrossRef]
20. Grabchenko, M.V.; Mamontov, G.V.; Zaikovskii, V.I.; La Parola, V.; Liotta, L.F.; Vodyankina, O.V. The role of metal-support interaction in Ag/CeO_2 catalysts for CO and soot oxidation. *Appl. Catal. B Environ.* **2020**, *260*, 118148. [CrossRef]
21. Xu, R.; Wang, X.; Wang, D.; Zhou, K.; Li, Y. Surface structure effects in nanocrystal MnO_2 and Ag/MnO_2 catalytic oxidation of CO. *J. Catal.* **2006**, *237*, 426–430. [CrossRef]
22. Liu, H.; Dai, X.; Wang, K.; Yan, Z.; Qian, L. Highly efficient catalysts of $Mn_{1-x}Ag_xCo_2O_4$ spinel oxide for soot combustion. *Catal. Commun.* **2017**, *101*, 134–137. [CrossRef]
23. Machocki, A.; Ioannides, T.; Stasinska, B.; Gac, W.; Avgouropoulos, G.; Delimaris, D.; Grzegorczyk, W.; Pasieczna, S. Manganese–lanthanum oxides modified with silver for the catalytic combustion of methane. *J. Catal.* **2004**, *227*, 282–296. [CrossRef]
24. Cui, B.; Zhou, K.; Hu, M.; Zhao, T.; Liu, Y.-Q.; Li, Y.; Shao, Z.; Zhao, M. The pivotal role of Ag species on porous nanosheets in the significant reduction of soot ignition temperature. *Chem. Eng. J.* **2023**, *461*, 142107. [CrossRef]
25. Chen, L.; Li, T.; Zhang, J.; Wang, J.; Chen, P.; Fu, M.; Wu, J.; Ye, D. Chemisorbed superoxide species enhanced the high catalytic performance of Ag/Co_3O_4 nanocubes for soot oxidation. *ACS Appl. Mater. Interfaces* **2021**, *13*, 21436–21449. [CrossRef]

26. Zhao, B.; Jin, B.; Wu, X.; Weng, D.; Ran, R. Ag-modified $SmMn_2O_5$ catalysts for CO and C_3H_8 oxidation. *Catal. Commun.* **2022**, *167*, 106456. [CrossRef]
27. Jin, B.; Zhao, B.; Liu, S.; Li, Z.; Li, K.; Ran, R.; Si, Z.; Weng, D.; Xiaodong, W. $SmMn_2O_5$ catalysts modified with silver for soot oxidation: Dispersion of silver and distortion of mullite. *Appl. Catal. B Environ.* **2020**, *273*, 119058. [CrossRef]
28. Ren, W.; Ding, T.; Wang, W.-L.; Zhang, Y.-X.; Li, Y.; Lu, Y.-T.; Ma, C. Microstructure and cation distribution of $Mn_{2-x}Al_xZn_{0.2}Ni_{0.6}Mg_{0.2}O_4$ high entropy oxide films. *J. Mater. Sci. Mater. Electron.* **2023**, *34*, 655. [CrossRef]
29. Shen, M.; Zhao, Z.; Chen, J.; Su, Y.; Wang, J.; Wang, X. Effects of calcium substitute in $LaMnO_3$ perovskites for NO catalytic oxidation. *J. Rare Earths* **2013**, *31*, 119–123. [CrossRef]
30. Du, P.; Song, L.; Xiong, J.; Cao, H.; Xi, Z.; Guo, S.; Wang, N.; Chen, J. Electrospinning fabrication and luminescent properties of $SrMoO_4$:Sm^{3+} nanofibers. *J. Alloys Compd.* **2012**, *540*, 179–183. [CrossRef]
31. Ma, C.; Ma, D.-K.; Yu, W.; Chen, W.; Huang, S. Ag and N-doped graphene quantum dots co-modified $CuBi_2O_4$ submicron rod photocathodes with enhanced photoelectrochemical activity. *Appl. Surf. Sci.* **2019**, *481*, 661–668. [CrossRef]
32. Zhu, Y.; Du, C.; Feng, Z.; Chen, Y.; Li, H.; Chen, R.; Shen, M.; Shan, B. Highly dispersed Pd on macroporous $SmMn_2O_5$ mullite for low temperature oxidation of CO and C_3H_8. *RSC Adv.* **2018**, *8*, 5459–5467. [CrossRef]
33. Chu, F.; Zuo, C.; Ma, C.; Tian, Z.; Feng, T.; Zhao, C.; Wang, Y.; Dong, W.; Long, J.; Wen, Z.; et al. Solution combustion synthesis of $La_xSm_{1-x}Mn_2O_5$ nanoparticles and their electrocatalytic performances for Al-air batteries. *Mater. Res. Bull.* **2018**, *108*, 16–22. [CrossRef]
34. Song, L.; Zhang, H.; Xiong, J.; Chen, Z.; Liu, Y.; Zhou, H.; Yang, W.; Cao, D.; Huang, H.; Chen, L.; et al. Doped Mn modulates the local charge distribution of cobalt-based spinel catalysts to promote the availability of ligand lattice oxygen for complete oxidation of methane. *Appl. Catal. B Environ.* **2024**, *343*, 123547. [CrossRef]
35. Park, J.Y.; Dong, W.J.; Jung, S.-M.; Kim, Y.-T.; Lee, J.-L. Oxygen reduction reaction of vertically-aligned nanoporous Ag nanowires. *Appl. Catal. B Environ.* **2021**, *298*, 120586. [CrossRef]
36. Clemens, K.; Shishkin, A.; Carlsson, P.; Skoglundh, M.; Martínez-Casado, F.; Matěj, Z.; Balmes, O.; Härelind, H. Reaction-driven ion exchange of copper into zeolite SSZ-13. *ACS Catal.* **2015**, *5*, 6209–6218. [CrossRef]
37. Chen, Y.; Shen, G.; Lang, Y.; Chen, R.; Jia, L.; Yue, J.; Shen, M.; Du, C.; Shan, B. Promoting soot combustion efficiency by strengthening the adsorption of NO_x on the 3DOM mullite catalyst. *J. Catal.* **2020**, *384*, 96–105. [CrossRef]
38. Feng, Z.; Liu, Q.; Chen, Y.; Zhao, P.; Peng, Q.; Cao, K.; Chen, R.; Shen, M.; Shan, B. Macroporous $SmMn_2O_5$ mullite for NO_x-assisted soot combustion. *Catal. Sci. Technol.* **2017**, *7*, 838–847. [CrossRef]
39. Chen, Y.; Du, C.; Lang, Y.; Jia, L.; Chen, R.; Shan, B. Carboxyl-modified colloidal crystal templates for the synthesis of three-dimensionally ordered macroporous $SMMN_2O_5$ mullite and its application in NO_x-assisted soot combustion. *Catal. Sci. Technol.* **2018**, *8*, 5955–5962. [CrossRef]
40. Nossova, L.; Caravaggio, G.; Couillard, M.; Ntais, S. Effect of preparation method on the performance of silver-zirconia catalysts for soot oxidation in diesel engine exhaust. *Appl. Catal. B Environ.* **2018**, *225*, 538–549. [CrossRef]
41. Huo, Z.; Zhao, P.; Miu, P.; Ren, L.; Tan, B.; Feng, N.; Wan, H.; Guan, G. Enhanced catalytic oxidation of soot over 3DOM $LaMnO_3$ by adding Ag and CeO_2: Improving the generation and delivery of active oxygen species. *Appl. Surf. Sci.* **2022**, *600*, 154204. [CrossRef]
42. Zhang, H.-L.; Zhu, Y.; Wang, S.-D.; Zhao, M.; Gong, M.-C.; Chen, Y.-Q. Activity and thermal stability of $Pt/Ce_{0.64}Mn_{0.16}R_{0.2}O_x$ (R = Al, Zr, La, or Y) for soot and NO oxidation. *Fuel Process. Technol.* **2015**, *137*, 38–47. [CrossRef]
43. Xu, H.; Zeng, L.; Cui, L.; Guo, W.; Gong, C.; Xue, G. In-situ generation of platinum nanoparticles on $LaCoO_3$ matrix for soot oxidation. *J. Rare Earths* **2022**, *40*, 888–896. [CrossRef]
44. Lee, J.; Jo, D.; Choung, J.; Kim, C.; Ham, H.; Lee, K.-Y. Roles of noble metals (M = Ag, Au, Pd, Pt and Rh) on CeO_2 in enhancing activity toward soot oxidation: Active oxygen species and DFT calculations. *J. Hazard. Mater.* **2021**, *403*, 124085. [CrossRef]
45. López-suárez, F.; Bueno-lópez, A.; Illán-gómez, M.; Adamski, A.; Ura, B.; Trawczynski, J. Copper catalysts for soot oxidation:alumina versus perovskite supports. *Environ. Sci. Technol.* **2008**, *42*, 7670–7675. [CrossRef] [PubMed]
46. Wang, M.; Zhang, Y.; Yu, Y.; Shan, W.; He, H. Insight into the better performance of Co than Pt on Ce-Sn catalyst for soot oxidation. *Fuel* **2023**, *346*, 128379. [CrossRef]
47. Piumetti, M.; Bensaid, S.; Russo, N.; Fino, D. Nanostructured ceria-based catalysts for soot combustion: Investigations on the surface sensitivity. *Appl. Catal. B Environ.* **2015**, *165*, 742–751. [CrossRef]
48. Wang, H.; Luo, S.; Zhang, M.; Liu, W.; Wu, X.; Liu, S. Roles of oxygen vacancy and O^- in oxidation reactions over CeO_2 and Ag/CeO_2 nanorod model catalysts. *J. Catal.* **2018**, *368*, 365–378. [CrossRef]
49. Wang, X.; Jin, B.; Feng, R.; Liu, W.; Weng, D.; Wu, X.; Liu, S. A robust core-shell silver soot oxidation catalyst driven by Co_3O_4: Effect of tandem oxygen delivery and Co_3O_4-CeO_2 synergy. *Appl. Catal. B Environ.* **2019**, *250*, 132–142. [CrossRef]
50. Tang, Z.; Chen, T.; Liu, K.; Du, H.; Podkolzin, S.G. Atomic, molecular and hybrid oxygen structures on silver. *Langmuir* **2021**, *37*, 11603–11610. [CrossRef]
51. Yang, J.; Zhang, J.; Liu, X.; Duan, X.; Wen, Y.; Chen, R.; Shan, B. Origin of the superior activity of surface doped $SmMn_2O_5$ mullites for NO oxidation: A first-principles based microkinetic study. *J. Catal.* **2018**, *359*, 122–129. [CrossRef]
52. Shimizu, K.; Katagiri, M.; Satokawa, S.; Satsuma, A. Sintering-resistant and self-regenerative properties of Ag/SnO_2 catalyst for soot oxidation. *Appl. Catal. B Environ.* **2011**, *108–109*, 39–46. [CrossRef]

53. Qu, Z.; Huang, W.; Cheng, M.; Bao, X. Restructuring and redispersion of silver on SiO_2 under oxidizing/reducing atmospheres and its activity toward CO oxidation. *J. Phys. Chem. B* **2005**, *109*, 15842–15848. [CrossRef] [PubMed]
54. Bukhtiyarov, A.; Stakheev, A.; Mytareva, A.; Prosvirin, I.; Bukhtiyarov, V. In situ XPS study of the size effect in the interaction of NO with the surface of the model Ag/Al_2O_3/FeCrAl catalysts. *Russ. Chem. Bull.* **2015**, *64*, 2780–2785. [CrossRef]